

The five parameter grain boundary character distribution of polycrystalline silicon

Sutatch Ratanaphan · Yohan Yoon ·
Gregory S. Rohrer

Received: 4 February 2014 / Accepted: 21 March 2014 / Published online: 8 April 2014
© Springer Science+Business Media New York 2014

Abstract The purpose of this paper is to describe the five-parameter grain boundary character distribution (GBCD) of polycrystalline silicon and compare it to distributions measured in metals and ceramics. The GBCD was determined from the stereological analysis of electron backscatter diffraction maps. The distribution of grain boundary disorientations is non-random and has peaks at 36° , 39° , 45° , 51° , and 60° . The axis-angle distribution reveals that most of the grain boundaries have misorientations around the [111], [110], and [100] axes. The most common grain boundary type (30 % number fraction) has a 60° misorientation around [111] and of these boundaries, the majority are twist boundaries. For other common boundaries, symmetric tilt configurations are preferred. The grain boundary character distribution of Si is distinct from those previously observed for metals and ceramics.

The measured grain boundary populations are inversely correlated to calculated grain boundary energies available in the literature.

Introduction

Polycrystalline silicon has been widely used for photovoltaic solar cells. Because of the tremendous demand for renewable solar power, efforts have been made to reduce the cost and improve the energy efficiency of polycrystalline Si photovoltaic cells [1–4]. It has been reported that electron–hole recombination rates are strongly influenced by the character of the grain boundary and depend on both the grain boundary misorientation and grain boundary plane orientation [5–7]. For example, small angle grain boundaries have higher recombination rates than large angle grain boundaries [5]. One exception is the coherent twin grain boundary, which is reported to be electrically inactive [5–7] and energetically stable [8, 9]. The coherent twin is the grain boundary with a misorientation of 60° around [111] and is terminated by (111) planes on either side of the boundary. In the commonly used coincident site lattice (CSL) notation, this is a $\Sigma 3$ boundary with a twist configuration. While $\Sigma 3$ incoherent twin boundaries with (110) and (112) planes were also electrically inactive in high-purity polycrystalline silicon, their electrical properties deteriorated in the presence of iron impurities [8]. To clarify the nomenclature used in this paper, we note that another common designation for the coherent twin is a 70.5° symmetric tilt about [110], which is structurally indistinguishable from the 60° twist around [111]. We uniformly chose to describe boundary crystallography by the representation in the fundamental zone, and in this case it is the twist representation. Furthermore, we will refer to all boundaries with the $\Sigma 3$ misorientation, but different grain

S. Ratanaphan · G. S. Rohrer (✉)
Department of Materials Science and Engineering, Carnegie
Mellon University, 5000 Forbes Avenue, Pittsburgh, PA 15213,
USA
e-mail: rohrer@cmu.edu

Present Address:
S. Ratanaphan
Department of Tool and Materials Engineering, King Mongkut's
University of Technology Thonburi, 126 Pracha Uthit Rd,
Thung Khru, Bangkok 10140, Thailand

Y. Yoon
Department of Materials Science and Engineering, North
Carolina State University, 911 Partners Way, Raleigh,
NC 27695, USA

Present Address:
Y. Yoon
National Institute of Standards and Technology, 100 Bureau Dr.,
Gaithersburg, MD 20899, USA

boundary plane orientations, as $\Sigma 3$ incoherent twin boundaries.

Because the electrical properties of grain boundaries in Si depend on both the grain boundary misorientation and grain boundary plane inclination, we seek a statistical description of the grain boundary population. It was reported that most boundaries in cast polycrystalline silicon are the $\Sigma 3$, $\Sigma 9$, and $\Sigma 27$ misorientation types [5]. However, these conclusions were based on a relatively small number of observations. Here, we measure the grain boundary character distribution (GBCD), which specifies the relative areas of grain boundaries as a function of lattice misorientation and grain boundary plane orientation over the entire range of possibilities [10]. While in the current paper, it is the grain boundary line length per area that is measured, this quantity is stereologically related to the area per volume [11]. A significant challenge associated with this work is that a statistically significant measure of the five-parameter GBCD requires a large number of observations. However, the cast polycrystalline Si used in photovoltaic applications has a large grain size and relatively few grain boundaries. Using a sample with a sub-millimeter grain size, we were able to characterize more than 23000 grain boundaries. By comparing results calculated using different amounts of data, we conclude that this is sufficient to accurately determine the populations of the most common grain boundaries.

The GBCDs of a wide range of polycrystalline materials have been measured over that past decade [12]. This includes metallically bonded materials with the FCC [13–17], BCC [18, 19], and HCP [20, 21] structures and a number of oxide ceramics [22–26] with predominantly ionic bonding. However, the five-parameter GBCD of a material with purely covalent bonding has not yet been measured. This is another motivation to measure the GBCD of polycrystalline Si. One of the common features of the GBCDs of metallic and ceramic materials is that the grain boundary distributions are inversely correlated to grain boundary energies [27]. This trend was even found for boundaries in block co-polymer systems that are governed by intermolecular forces [28]. Considering this, it seems likely that the trend should persist in polycrystalline silicon, in which the interactions across grain boundaries are governed by covalent bonds. Therefore, the main points of this paper are to describe the relative grain boundary populations in covalently bonded polycrystalline Si, to compare them to measurements in metals and ceramics, and to compare the populations to calculated Si grain boundary energies.

Experimental

Cast polycrystalline silicon was obtained from MEMC (St. Peters, MO, USA). The Si was boron-doped with a

concentration of $5.5 \times 10^{16} \text{ cm}^{-3}$. A wafer was cut with a wire saw and etched in potassium hydroxide solution ($\text{KOH}:\text{H}_2\text{O} = 1:1$) to remove surface damage. This surface was suitable for electron backscatter diffraction (EBSD) analysis without further treatment. EBSD mapping was carried out using a field-emission gun SEM (Quanta 200, FEI Company). For each measurement, the sample was tilted to about 70° with respect to the electron beam. The EBSD measurement was carried out using an accelerating voltage of 20 kV and a step size of 5 μm . Standard clean-up procedures in the TSL software were used to remove incorrectly indexed pixels. First, a neighbor confidence index (CI) correction was used to change all of the pixels with CI less than 0.1 to the orientation and CI of the neighbor with the highest CI. Second, a grain CI standardization was used to change the CIs of all points in a grain to the maximum CI found in the grain. Next, the single iteration grain dilation was used with a minimum grain size of 50 pixels and a tolerance angle of 5° . Using this procedure, fewer than 2 % of the data points were changed. Next, individual orientations inside the grain were changed to a value equal to the average orientation of all pixels within the grain. The reconstructed grain boundary line segments, used in the stereological GBCD calculation, were extracted from 26 fields of view using the TSL/OIM software. These images covered the entire region of the ingot that contained sub-millimeter sized grains. To approximate the grain boundary positions, straight lines were used to connect all of the triple junctions. If these line segments deviated from the grain boundary plane by more than two pixels, the segments were subdivided to better match the curvatures of grain boundaries [29]. We have found that a tolerance of two pixels best approximates the boundary curvature, while not reproducing noise and the shape of the hexagonal scan grid. This was applied to all boundaries and is a necessary step because grain boundaries with different orientations are classified differently. The GBCD was calculated from 23157 line segments using the stereological method described in Ref. [27] with a binning resolution of 10° .

Results

Representative EBSD maps of polycrystalline Si before and after clean-up are shown in Fig. 1a, b, respectively. The image after clean-up has reconstructed grain boundary line segments overlaid in black. The microstructure consisted of equiaxed grains containing multiple twin lamellae (the straight parallel lines). The average grain size was 290 μm . The sample showed no grain orientation texture; the maxima in the inverse pole figures (not shown) were less than 1.5 MRD.

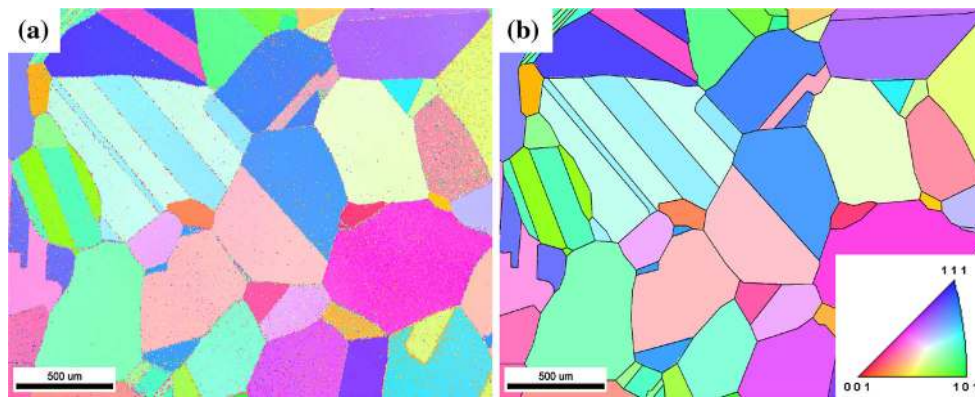


Fig. 1 Orientation map of the polycrystalline silicon specimen, **a** raw EBSD map before clean-up, **b** cleaned map with reconstructed grain boundary line segments (black lines) superimposed. The

crystallographic orientations are colored according to the standard stereographic triangle on the right in **b**

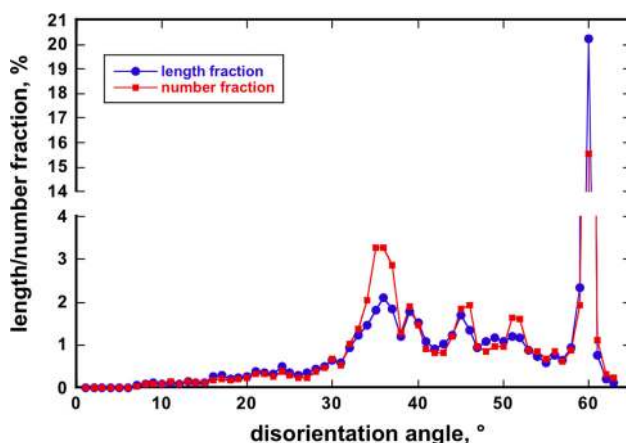


Fig. 2 Disorientation angle distribution for 23157 grain boundaries in Si. Squares indicate the number fraction of grain boundaries and the circles indicate the length fraction. Note the break in the vertical axis to emphasize the smaller peaks in comparison to the dominant peak at 60°

The grain boundary population as a function of disorientation angle (disorientation refers to the minimum of all equivalent misorientation angles) is shown in Fig. 2. Note that the values of the distribution below 5° are exactly zero, because this was the threshold used to define a boundary between two orientations. The distribution is discretized with a resolution of 1°. With 58 non-trivial bins, this means that there are, on average, about 400 grain boundaries per bin. There are obvious peaks at 36°, 39°, 45°, 51°, and 60°.

The misorientation axis-angle distribution was calculated to determine the relevant misorientation axes at each of the peaks in Fig. 2. In this case, a discretization of 5° was used. At this level of discretization, there are about 91 distinct axis-angle pairs and, on average, about 250 observations per boundary type. The grain boundary distribution in axis-angle space is shown in Fig. 3 for each of

the largest peaks in Fig. 2. The second largest peak in Fig. 2 is at 36° and the distribution at this angle is shown in Fig. 3a. Obvious peaks are present at the [100] and [110] orientations. Note that the distributions at 36° and 39° are nearly the same (Fig. 3b). This is because of the relatively coarse discretization of the distribution. There are several relatively low Σ coincident site lattice (CSL) boundaries in this angular range: $\Sigma 27b$ at 35.4° around [210], $\Sigma 5$ at 36.9° around [100], and $\Sigma 9$ at 38.9° around [110]. Considering this, the peak at [100] can be assigned to $\Sigma 5$ boundaries and the peak at [110] is from $\Sigma 9$ boundaries. However, there is no indication that the $\Sigma 27b$ boundary has a significant population.

Grain boundaries with the 45° disorientation mainly correspond to rotations around [100]. This is close to the $\Sigma 29a$ misorientation (43.6° around [100]), so we will designate this boundary as $\Sigma 29a$. This point is the end of the fundamental zone for rotations about [100]. Larger rotations about this axis signify misorientations that are indistinguishable from those at angles less than 45°. For example, the grain boundary with a 51° misorientation around [100] is the same as 39° around [100]. Therefore, the peak at 51° around [100] corresponds to the same boundaries that created the peak at 39°. The other local maxima at 51°, however, represent unique grain boundaries. The local maximum at [110] corresponds to the $\Sigma 11$ boundary (50.5° around [110]). The local maximum at (111) corresponds approximately to the $\Sigma 19b$ misorientation (46.8° around [111]). There is also a peak near the [321] axis that is not close to any CSL with $\Sigma \leq 29$. Finally, the distribution of axes at 60° has a single maximum at the [111] orientation. This corresponds to the $\Sigma 3$ misorientation of coherent twin boundaries.

Knowing where the maxima are in misorientation space, it is now possible to examine the grain boundary plane distributions at these misorientations. While the

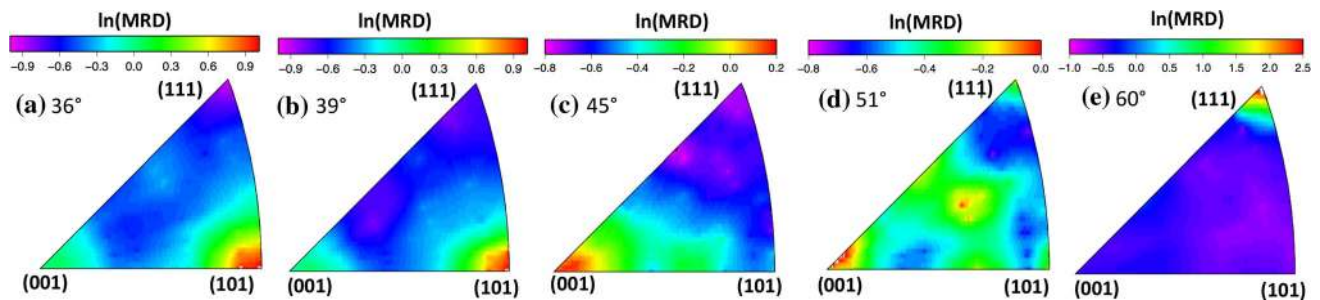


Fig. 3 Distributions of misorientation axes for grain boundaries in Si. The resolution is 5° and the length fractions are plotted using a logarithmic scale

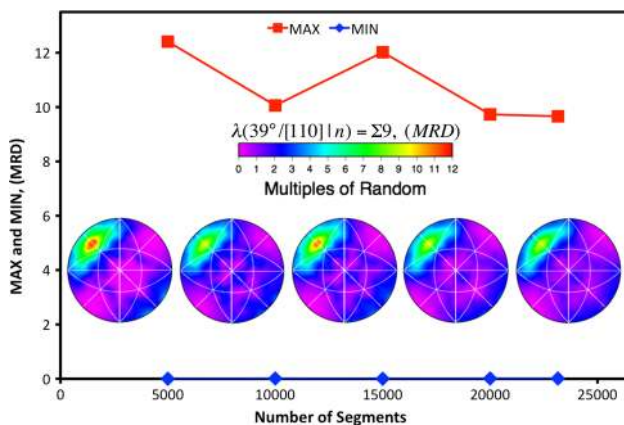


Fig. 4 Maxima and minima of the grain boundary plane distribution for $\Sigma 9$ grain boundaries as a function of the number of segments used to compute the distribution. The insets show stereographic projections of the grain boundary plane distributions calculated from 5000, 10000, 15000, 20000, and 23157 segments, respectively

distributions illustrated in Figs. 2 and 3 were determined directly from the measurements, the grain boundary plane distribution requires a stereological interpretation of the data. Ideally, we would like to have 50000 grain boundary observations to compute the distribution [11]. However, this number assumes a relatively random misorientation distribution. Because nearly all of the data are found at only five different misorientation angles, the computed plane distributions at these misorientations are likely to be accurate. To test this idea, we computed the grain boundary plane distributions using different subsets of the data, and compared the results. An example is illustrated in Fig. 4. In this case, the grain boundary plane distribution was calculated with a resolution of 10° for $\Sigma 9$ grain boundaries using 5000, 10000, 15000, 20000, and 23157 line segments. The maxima and minima of the distribution are also shown as a function of the number of grain boundaries and the resulting grain boundary plane distributions are shown in the inset. From these results, we first conclude that the overall shape of the distribution, including the location of

the maximum, is not sensitive to the number of lines segments. Second, for more than 10000 line segments, the value at the maximum fluctuates within a range of $\pm 10\%$. This analysis was repeated for the four boundaries of interest and the same results were obtained. Furthermore, the calculations were repeated for a lower resolution (12.5°). Using the lower resolution, there are fewer distinct grain boundary types, so less data are required. When the results from 10° to 12.5° were compared, there were no significant differences in the distributions.

Based on the calculations described above, we concluded that the calculated grain boundary plane distributions for the most populated grain boundaries are reliable within an uncertainty of about $\pm 10\%$. The distribution of grain boundary planes for boundaries corresponding to the local maxima in Fig. 3 is shown in Fig. 5. The grain boundary plane distribution at the $\Sigma 5$ misorientation (36° around $[100]$), illustrated in Fig. 5a, has peaks at the positions of the symmetric tilt boundaries made up of $(0\bar{1}2)$ planes. Similarly, the grain boundary plane distribution at the $\Sigma 9$ misorientation (39° around $[110]$), illustrated in Fig. 5b, has its maximum at the position of the symmetric tilt boundary with $(\bar{2}21)$ planes. The grain boundary plane distribution at 45° around $[100]$ (Fig. 5c) also has maxima that include the symmetric tilts. However, the true maxima occur for mixed boundaries terminated by $\{112\}$ type planes. The grain boundary plane distribution at the $\Sigma 11$ misorientation (51° around $[110]$) is illustrated in Fig. 5d. At this misorientation, the symmetric tilt boundary with $(\bar{2}23)$ planes has the maximum population. Finally, the global maximum of the distribution occurs for the coherent twin grain boundary, which is a twist boundary with the $\Sigma 3$ misorientation (60° around $[111]$).

Discussion

Consistent with previous studies [5, 7], our results show that $\Sigma 3$ grain boundaries make up the largest fraction of all grain boundaries in polycrystalline Si. Using Brandon's

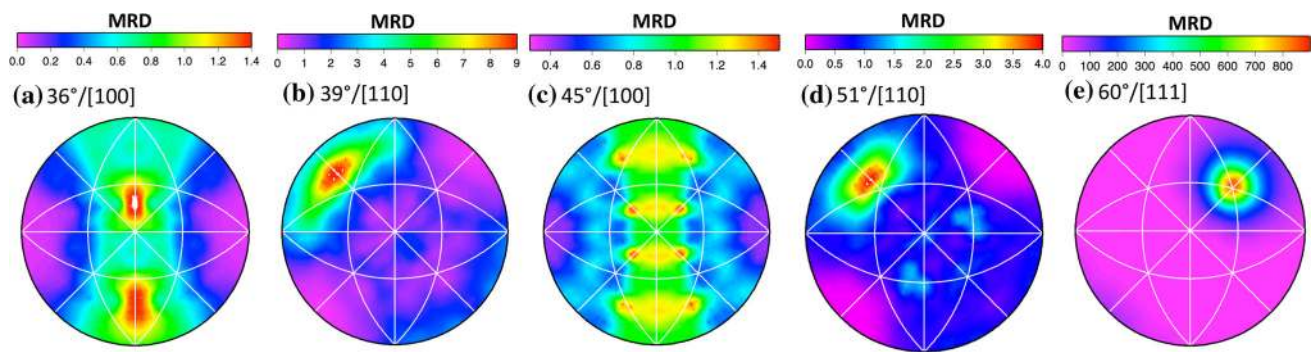


Fig. 5 Grain boundary plane distributions for boundaries corresponding to the local maxima in the misorientation distribution shown in Fig. 3. The distributions are plotted in stereographic projection,

with the [001] direction normal to the page and the [100] direction *horizontally* and to the *right*

[30] criterion, they make up 29.6 % (percentage by number) of all boundaries, which is consistent with the previous studies [5]. Boundaries with the $\Sigma 5$, $\Sigma 9$, $\Sigma 11$, and $\Sigma 29a$ misorientations make up other local maxima in the distribution. One possible reason for the high population of $\Sigma 9$ boundaries is that they are a natural consequence of the high population of $\Sigma 3$ boundaries. The geometric consequence of two $\Sigma 3$ boundaries meeting is a $\Sigma 9$ boundary to complete the triple junction [31]. If the $\Sigma 3$ boundaries mixed randomly, one would expect the concentration of $\Sigma 9$ boundaries to be equal to the square of the concentration of $\Sigma 3$ boundaries. Recognizing that some of the $\Sigma 3$ grain boundary segments are part of the internal twin structure, we consider that only those $\Sigma 3$ segments that meet at triple junctions (23 % of all boundaries) would produce a $\Sigma 9$ boundary. In fact, the concentration of $\Sigma 9$ boundaries (5.4 %, number fraction, using Brandon's [30] criterion) is approximately equal to the concentration predicted by random mixing ($0.23^2 = 0.053$). This indicates that the population of $\Sigma 9$ boundaries is primarily the result of $\Sigma 3$ boundaries intersecting at random. It should also be noted that there is no evidence for a significant population of $\Sigma 27a$ or $\Sigma 27b$ boundaries. Materials containing high populations of $\Sigma 3$ and $\Sigma 9$ boundaries frequently have elevated populations of $\Sigma 27$ boundaries that form as a crystallographic consequence of the intersection of $\Sigma 3$ and $\Sigma 9$ boundaries [31], but this is not observed here.

The high population of $\Sigma 3$ grain boundaries is consistent with the GBCDs of many FCC metals that have been studied in the past [13, 14, 16, 32, 33]. However, there are also significant differences. Three notable differences are in the distribution of grain boundaries around the [111], [110], and [100] axes. In FCC materials, there is a relatively high population of [111] twist boundaries at all misorientations. However, in Si, it is only the twin boundary at the $\Sigma 3$ misorientation (60° around [111]) that has a significant population. The high population of

boundaries with [110] misorientations is consistent with FCC materials, but the distribution of grain boundary planes is not. In FCC materials, there is a relatively high population of grain boundaries for all tilt boundaries, with the maximum being reached at the orientation of the $(1\bar{1}n)$ symmetric tilt boundary (for example, $(1\bar{1}4)$ for $\Sigma 9$). However, in Si, the only measurable population is concentrated on the $(\bar{h}hn)$ symmetric tilt boundaries (for example, $(\bar{2}21)$ for $\Sigma 9$). Finally, the third significant difference is that in FCC metals there are very few boundaries with [100] misorientations. However, there are notable populations of certain [100] misorientated boundaries in Si. So, while the presence of twins in Si is similar to FCC metals, the distinct crystal structure of Si leads to a different GBCD. These differences are likely related to the differences in bonding interactions at the boundaries that lead to distinct atomic structures [34–37].

Based on previous studies of ceramics and metals, the grain boundary character distribution is thought to be determined by the anisotropy of the grain boundary energy [27, 38, 39]. In fact, there is an inverse correlation between the quantities and the same thing might be expected in Si. However, one significant difference is that the grain boundary networks in previous studies are formed by grain growth, following sintering or recrystallization. The Si examined here was formed by casting. It has been reported that the very straight (111) habit planes for the coherent twin boundary, as observed here, are a characteristic of cast, polycrystalline Si [40]. Therefore, the grain shapes are likely determined when the growing crystals impinge during solidification [40, 41]. Even so, at the high temperature at which impingement occurs, it is reasonable to assume that the interfaces are in local thermodynamic equilibrium as they are during grain growth.

To test for a relation between grain boundary population and energy, we will use calculated values of the grain boundary energy that are available in the literature. There

Table 1 The grain boundary energies [39, 41–43, 52] and grain boundary populations, which are shown in Fig. 6

θ	Σ	Boundary plane	Energy (J/m ²)	Population (MRD)
12.68	41	(4,5,0)	1.094	0.4
16.26	25	(3,4,0)	1.172	0.52
22.62	13	(2,3,0)	1.213	0.564
28.07	17	(3,5,0)	1.254	0.878
36.87	5	(1,2,0)	1.001	1.396
46.4	29	(2,5,0)	1.239	1.313
53.13	5	(1,3,0)	0.942	0.749
61.93	17	(1,4,0)	1.31	0.595
67.38	13	(1,5,0)	1.422	0.292
73.74	25	(1,7,0)	1.407	0.308
77.32	41	(1,9,0)	1.321	0.229
16.1	51	(1,−5,5)	0.956	1.112
20.05	33	(1,−4,4)	1.022	0.632
26.53	19	(1,−3,3)	0.787	0.647
31.59	27	(2,−5,5)	0.891	16.56
38.94	9	(1,−2,2)	0.661	12.083
45.98	59	(3,−5,5)	0.929	4.825
50.48	11	(2,−3,3)	0.951	4.588
55.88	41	(3,−4,4)	1.022	3.701
70.53	3	(1,1,1)	0.032	884.7
93.37	17	(3,−2,2)	1.022	0.548
109.47	3	(2,−1,1)	1.022	0
121.01	33	(5,−2,2)	1.339	0.122
129.52	11	(3,−1,1)	0.956	0.528
141.06	9	(4,−1,1)	1.317	1.484
148.41	27	(5,−1,1)	1.18	0.367
159.95	33	(8,−1,1)	1.519	0.651
13.17	19	(1,1,1)	2.164	0.811
15.18	43	(1,1,1)	2.296	0
16.43	49	(1,1,1)	2.507	0.811
17.9	31	(1,1,1)	2.427	0.583
21.79	7	(1,1,1)	2.322	0.908
27.8	13	(1,1,1)	2.533	0.287

have been many calculations of grain boundary energies using a range of techniques [42–44]. For consistency, we use here a set of grain boundary energies that result from tight-binding calculations and includes 11 [100] symmetric tilt boundaries [45], 16 [110] symmetric tilt boundaries [34, 43], and 6 (111) twist boundaries [46]. These energies are listed in Table 1. Within this data set, the minimum and maximum grain boundary energies are those of the coherent twin boundary (0.032 J/m²) and the Σ 13 (111) twist boundary (2.53 J/m²), respectively. To test for a correlation between the measured populations and the calculated grain boundary energies, we plot (in Fig. 6) the

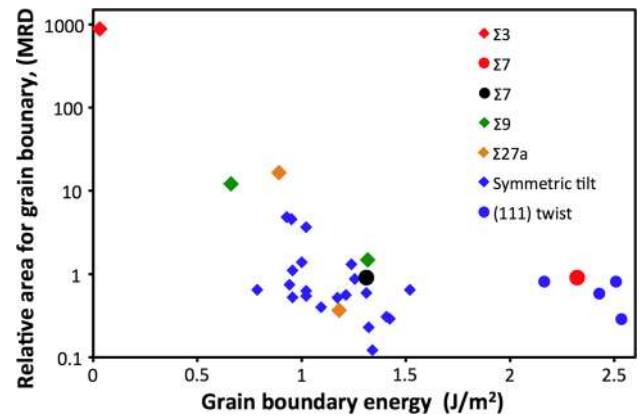


Fig. 6 The relationship between grain boundary populations and calculated grain boundary energies in Si [34, 43, 45, 46, 56]. The horizontal axis shows the calculated boundary energies, while the vertical axis shows the relative grain boundary areas for the same boundary. The grain boundaries are separated into two categories: tilt boundaries (diamonds) and twist boundaries (circles). Note that the relative energies of the Σ 7 (111) twist boundary calculated by using the tight-binding method [46] (red) and the transferable semi empirical tight-binding method [47] (black) and are shown with the large solid circles

logarithm of the measured relative area as a function of the calculated grain boundary energies. The maxima in the grain boundary plane distribution for the Σ 3 and Σ 9 misorientations, which are centered at (111) and ($\bar{2}21$) planes in Fig. 5e, b, respectively, correspond to the lowest boundary energies for these misorientations (see Table 1). The overall trend suggests a moderate negative correlation between the relative energies and the grain boundary areas, as seen in other materials. Note that the logarithmic distribution indicates the same functional form as the Boltzmann distribution. It has been previously suggested that grain boundary populations approach this distribution during grain growth through a mechanism that preferentially eliminates higher energy grain boundaries from the population as the total interface area decreases [38].

It is clear that if the six highest energy data points, which all correspond to (111) twist boundaries (except for the twin), were removed, then the correlation would improve. In fact, when these points are removed, the correlation coefficient changes from -0.41 to -0.72 , indicating a moderate negative correlation with these points included and a strong negative correlation without them. Considering this, the inverse correlation between calculated grain boundary energies and relative energies in Si is similar to what has been observed in metals and ceramics [12, 27].

One potential difficulty in accurately calculating the highest energy grain boundaries in Si (such as the (111) twist boundaries) is constructing them with the correct structure [47]. In fact, this point has been made by von

Alfthan et al. [37], who showed that the energies of $\Sigma 5$ twist boundaries could vary by 30 %, depending on the assumed structure. In this context, it is interesting to note that when the boundary energy of the $\Sigma 7$ (111) twist boundary was calculated using an improved model, it was substantially lower in energy (1.31 J/m^2) than the original value of 2.32 J/m^2 [47]. The energy that resulted from the improved calculation is marked by the black circle on Fig. 6 and is consistent with the trend found for the lower energy grain boundaries. If we presume that the other five (111) twist boundaries were similarly overestimated as the $\Sigma 7$ was, then the inverse correlation between the area and energy would be much stronger.

It has been reported that high-energy grain boundaries in silicon lower their boundary energy by introducing an amorphous-like structure at the grain boundary associated with the reduction in the numbers of dangling bonds [44, 46, 48–52]. However, the work of von Alfthan et al. [37, 53] suggests that the structures of certain twist boundaries ($\Sigma 25$, $\Sigma 5$, and $\Sigma 29$) remain ordered up to the melting point. These contradictions point to the difficulty of modeling the correct atomic structure for these grain boundaries. Therefore, it is plausible to assume that the simulated energies for the highest energy grain boundaries may not represent the equilibrium state [47, 54]. Furthermore, there is also evidence that structural transitions occur with temperature [53], suggesting that distinct grain boundary complexions may occur with distinct energies for the same boundary type at different temperatures [55].

Conclusion

The grain boundary character distribution in Si is highly anisotropic. The five most common boundaries are the $\Sigma 3$ ($60^\circ/[111]$) (111) twist boundary at 900 MRD, the $\Sigma 5$ ($36^\circ/[100]$) ($\bar{1}20$) symmetric tilt boundary at 1.5 MRD, the $\Sigma 9$ ($39^\circ/[110]$) ($\bar{2}21$) symmetric tilt at 10 MRD, the $\Sigma 11$ ($51^\circ/[110]$) ($\bar{2}23$) symmetric tilt boundary at 4 MRD, and the $\Sigma 29a$ ($45^\circ/[100]$) (112) mixed boundary at 1.5 MRD. Nearly all [110] and [100] misorientations favor symmetric tilt configurations. The high population of coherent twin boundaries is consistent with what is found in metals, but the populations at other misorientations are distinct. The measured grain boundary populations are inversely correlated with the calculated grain boundary energies.

Acknowledgements The work at Carnegie Mellon was supported by the MRSEC program of the National Science Foundation under Award Number DMR-0520425. S.R. Acknowledges the Higher Educational Strategic Scholarship for Frontier Research Network from The Commission on Higher Education, Thailand. All of the authors acknowledge the assistance of Prof. George Rozgonyi of NCSU.

References

1. Bahrami A, Mohammadnejad S, Soleimaninezhad S (2013) Photovoltaic cells technology: principles and recent developments. *Opt Quant Electron* 45:161–197. doi:[10.1007/s11082-012-9613-9](https://doi.org/10.1007/s11082-012-9613-9)
2. Saga T (2010) Advances in crystalline silicon solar cell technology for industrial mass production. *NPG Asia Mat* 2:96–102. doi:[10.1038/asiamat.2010.82](https://doi.org/10.1038/asiamat.2010.82)
3. Shah A, Torres P, Tscharnner R, Wyrsh N, Keppner H (1999) Photovoltaic technology: the case for thin-film solar cells. *Science* 285:692–698. doi:[10.1126/science.285.5428.692](https://doi.org/10.1126/science.285.5428.692)
4. M Tanaka (2013) Recent progress in crystalline silicon solar cells. *IEICE Electronics Express* 10:1–12. doi:[10.1587/elex.10.20132006](https://doi.org/10.1587/elex.10.20132006)
5. J Chen, T Sekiguchi (2007) Carrier recombination activity and structural properties of small-angle grain boundaries in multicrystalline silicon. *Jpn J Appl Phys Part 1* 46:6489–6497. doi:[10.1143/jjap.46.6489](https://doi.org/10.1143/jjap.46.6489)
6. Tsurekawa S, Kido K, Watanabe T (2007) Interfacial state and potential barrier height associated with grain boundaries in polycrystalline silicon. *Mater Sci Eng A* 462:61–67. doi:[10.1016/j.msea.2006.02.471](https://doi.org/10.1016/j.msea.2006.02.471)
7. Wang ZJ, Tsurekawa S, Ikeda K, Sekiguchi T, Watanabe T (1999) Relationship between electrical activity and grain boundary structural configuration in polycrystalline silicon. *Interface Sci* 7:197–205. doi:[10.1023/a:1008796005240](https://doi.org/10.1023/a:1008796005240)
8. B Chen, J Chen, T Sekiguchi, M Saito, K Kimoto (2009) Structural characterization and iron detection at Sigma 3 grain boundaries in multicrystalline silicon. *J Appl Phys* 105:113502. doi:[10.1063/1.3129583](https://doi.org/10.1063/1.3129583)
9. Chen J, Sekiguchi T, Yang D, Yin F, Kido K, Tsurekawa S (2004) Electron-beam-induced current study of grain boundaries in multicrystalline silicon. *J Appl Phys* 96:5490–5495. doi:[10.1063/1.1797548](https://doi.org/10.1063/1.1797548)
10. Rohrer GS, Saylor DM, El Dasher B, Adams BL, Rollett AD, Wynblatt P (2004) The distribution of internal interfaces in polycrystals. *Zeitschrift Fur Metallkunde* 95:197–214
11. Saylor DM, El-Dasher BS, Adams BL, Rohrer GS (2004) Measuring the five-parameter grain-boundary distribution from observations of planar sections. *Metall Mater Trans A-Phys Metall Mat Sci* 35:1981–1989
12. Rohrer GS (2011) Measuring and interpreting the structure of grain-boundary networks. *J Am Ceram Soc* 94:633–646. doi:[10.1111/j.1551-2916.2011.04384.x](https://doi.org/10.1111/j.1551-2916.2011.04384.x)
13. Kim CS, Hu Y, Rohrer GS, Randle V (2005) Five-parameter grain boundary distribution in grain boundary engineered brass. *Scripta Mater* 52:633–637. doi:[10.1016/j.scriptamat.2004.11.025](https://doi.org/10.1016/j.scriptamat.2004.11.025)
14. Li J, Dillon SJ, Rohrer GS (2009) Relative grain boundary area and energy distributions in nickel. *Acta Mater* 57:4304–4311. doi:[10.1016/j.actamat.2009.06.004](https://doi.org/10.1016/j.actamat.2009.06.004)
15. Rohrer GS, Holm EA, Rollett AD, Foiles SM, Li J, Olmsted DL (2010) Comparing calculated and measured grain boundary energies in nickel. *Acta Mater* 58:5063–5069. doi:[10.1016/j.actamat.2010.05.042](https://doi.org/10.1016/j.actamat.2010.05.042)
16. Rohrer GS, Randle V, Kim CS, Hu Y (2006) Changes in the five-parameter grain boundary character distribution in alpha-brass brought about by iterative thermomechanical processing. *Acta Mater* 54:4489–4502. doi:[10.1016/j.actamat.2006.05.035](https://doi.org/10.1016/j.actamat.2006.05.035)
17. Saylor DM, El Dasher BS, Rollett AD, Rohrer GS (2004) Distribution of grain boundaries in aluminum as a function of five macroscopic parameters. *Acta Mater* 52:3649–3655. doi:[10.1016/j.actamat.2004.04.018](https://doi.org/10.1016/j.actamat.2004.04.018)
18. Beladi H, Rohrer GS (2013) The relative grain boundary area and energy distributions in a ferritic steel determined from three-

- dimensional electron backscatter diffraction maps. *Acta Mater* 61:1404–1412. doi:[10.1016/j.actamat.2012.11.017](https://doi.org/10.1016/j.actamat.2012.11.017)
19. Liu X, Choi D, Beladi H, Nuhfer NT, Rohrer GS, Barmak K (2013) The five-parameter grain boundary character distribution of nanocrystalline tungsten. *Scripta Mater* 69:413–416. doi:[10.1016/j.scriptamat.2013.05.046](https://doi.org/10.1016/j.scriptamat.2013.05.046)
 20. Kim CS, Massa TR, Rohrer GS (2008) Interface character distributions in WC-Co composites. *J Am Ceram Soc* 91:996–1001. doi:[10.1111/j.1551-2916.2007.02226.x](https://doi.org/10.1111/j.1551-2916.2007.02226.x)
 21. Randle V, Rohrer GS, Hu Y (2008) Five-parameter grain boundary analysis of a titanium alloy before and after low-temperature annealing. *Scripta Mater* 58:183–186. doi:[10.1016/j.scriptamat.2007.09.044](https://doi.org/10.1016/j.scriptamat.2007.09.044)
 22. Dillon SJ, Helmick L, Miller HM et al (2011) The orientation distributions of lines, surfaces, and interfaces around three-phase boundaries in solid oxide fuel cell cathodes. *J Am Ceram Soc* 94:4045–4051. doi:[10.1111/j.1551-2916.2011.04673.x](https://doi.org/10.1111/j.1551-2916.2011.04673.x)
 23. Dillon SJ, Rohrer GS (2009) Characterization of the grain-boundary character and energy distributions of Yttria using automated serial sectioning and EBSD in the FIB. *J Am Ceram Soc* 92:1580–1585. doi:[10.1111/j.1551-2916.2009.03064.x](https://doi.org/10.1111/j.1551-2916.2009.03064.x)
 24. Saylor DM, Morawiec A, Adams BL, Rohrer GS (2000) Misorientation dependence of the grain boundary energy in magnesia. *Interface Sci* 8:131–140
 25. Saylor DM, Morawiec A, Rohrer GS (2002) Distribution and energies of grain boundaries in magnesia as a function of five degrees of freedom. *J Am Ceram Soc* 85:3081–3083
 26. Saylor DM, Morawiec A, Rohrer GS (2003) Distribution of grain boundaries in magnesia as a function of five macroscopic parameters. *Acta Mater* 51:3663–3674. doi:[10.1016/S1359-6454\(03\)00181-2](https://doi.org/10.1016/S1359-6454(03)00181-2)
 27. Rohrer G (2011) Grain boundary energy anisotropy: a review. *J Mater Sci* 46:5881–5895. doi:[10.1007/s10853-011-5677-3](https://doi.org/10.1007/s10853-011-5677-3)
 28. HJ Ryu, DB Fortner, GS Rohrer, MR Bockstaller (2012) Measuring relative grain-boundary energies in block-copolymer microstructures. *Phys Rev Lett* 108:107801. doi:[10.1103/PhysRevLett.108.107801](https://doi.org/10.1103/PhysRevLett.108.107801)
 29. Wright SI, Larsen RJ (2002) Extracting twins from orientation imaging microscopy scan data. *J Microsc-Oxf* 205:245–252. doi:[10.1046/j.1365-2818.2002.00992.x](https://doi.org/10.1046/j.1365-2818.2002.00992.x)
 30. Brandon DG (1966) Structure of high-angle grain boundaries. *Acta Metall* 14:1479–1484
 31. Miyazawa K, Iwasaki Y, Ito K, Ishida Y (1996) Combination rule of Sigma values at triple junctions in cubic polycrystals. *Acta Cryst A* 52:787–796. doi:[10.1107/s0108767396005934](https://doi.org/10.1107/s0108767396005934)
 32. Randle V, Rohrer GS, Miller HM, Coleman M, Owen GT (2008) Five-parameter grain boundary distribution of commercially grain boundary engineered nickel and copper. *Acta Mater* 56:2363–2373. doi:[10.1016/j.actamat.2008.01.039](https://doi.org/10.1016/j.actamat.2008.01.039)
 33. Rohrer GS, Li J, Lee S, Rollett AD, Groeber M, Uchic MD (2010) Deriving grain boundary character distributions and relative grain boundary energies from three-dimensional EBSD data. *Mater Sci Technol* 26:661–669. doi:[10.1179/026708309X12468927349370](https://doi.org/10.1179/026708309X12468927349370)
 34. Kohyama M, Yamamoto R, Doyama M (1986) Reconstructed structures of symmetrical (011) tilt grain-boundaries in silicon. *Phys Status Solidi B* 138:387–397. doi:[10.1002/pssb.2221380202](https://doi.org/10.1002/pssb.2221380202)
 35. Paxton AT, Sutton AP (1988) A simple theoretical approach to grain-boundaries in silicon. *J Phys C* 21:L481–L488. doi:[10.1088/0022-3719/21/15/001](https://doi.org/10.1088/0022-3719/21/15/001)
 36. Paxton AT, Sutton AP (1989) A tight-binding study of grain boundaries in silicon. *Acta Metall* 37:1693–1715. doi:[10.1016/0001-6160\(89\)90056-4](https://doi.org/10.1016/0001-6160(89)90056-4)
 37. S von Alfhthan, PD Haynes, K Kaski, AP Sutton (2006) Are the structures of twist grain boundaries in silicon ordered at 0 K?. *Phys Rev Lett* 96:055505. doi:[10.1103/PhysRevLett.96.055505](https://doi.org/10.1103/PhysRevLett.96.055505)
 38. Dillon SJ, Rohrer GS (2009) Mechanism for the development of anisotropic grain boundary character distributions during normal grain growth. *Acta Mater* 57:1–7. doi:[10.1016/j.actamat.2008.08.062](https://doi.org/10.1016/j.actamat.2008.08.062)
 39. Gruber J, George DC, Kuprat AP, Rohrer GS, Rollett AD (2005) Effect of anisotropic grain boundary properties on grain boundary plane distributions during grain growth. *Scripta Mater* 53:351–355. doi:[10.1016/j.scriptamat.2005.04.004](https://doi.org/10.1016/j.scriptamat.2005.04.004)
 40. Fujiwara K, Tsumura S, Tokairin M et al (2009) Growth behavior of faceted Si crystals at grain boundary formation. *J Cryst Growth* 312:19–23. doi:[10.1016/j.jcrysgro.2009.09.055](https://doi.org/10.1016/j.jcrysgro.2009.09.055)
 41. Tandjaoui A, Mangelinck-Noel N, Reinhart G, Billia B, Guichard X (2013) Twinning occurrence and grain competition in multi-crystalline silicon during solidification. *CR Phys* 14:141–148. doi:[10.1016/j.crhy.2012.12.001](https://doi.org/10.1016/j.crhy.2012.12.001)
 42. Kohyama M (2002) Computational studies of grain boundaries in covalent materials. *Modell Simul Mater Sci Eng* 10:R31–R39. doi:[10.1088/0965-0393/10/3/202](https://doi.org/10.1088/0965-0393/10/3/202)
 43. Kohyama M, Yamamoto R, Doyama M (1986) Structures and energies of symmetrical 011 tilt grain boundaries in silicon. *Phys Status Solidi B-Basic Res* 137:11–20. doi:[10.1002/pssb.2221370102](https://doi.org/10.1002/pssb.2221370102)
 44. Phillpot SR, Wolf D (1989) Structure-energy correlation for grain boundaries in silicon. *Philos Mag A-Phys Condens Matter Struct Defects Mech Prop* 60:545–553
 45. Kohyama M (1987) Structures and energies of symmetrical <001> tilt grain-boundaries in silicon. *Phys Status Solidi B* 141:71–83. doi:[10.1002/pssb.2221410106](https://doi.org/10.1002/pssb.2221410106)
 46. Kohyama M, Yamamoto R, Doyama M (1986) Energies and structures of (111) coincidence twist boundaries in 3C-SiC, diamond, and silicon. *Phys Status Solidi B* 136:31–36. doi:[10.1002/pssb.2221360103](https://doi.org/10.1002/pssb.2221360103)
 47. Kohyama M, Yamamoto R (1994) Tight-binding study of grain-boundaries in Si – energies and atomic structure of twist grain-boundaries. *Phys Rev B* 49:17102–17117. doi:[10.1103/PhysRevB.49.17102](https://doi.org/10.1103/PhysRevB.49.17102)
 48. Cleri F (2001) Atomic and electronic structure of high-energy grain boundaries in silicon and carbon. *Comput Mater Sci* 20:351–362. doi:[10.1016/s0927-0256\(00\)00194-4](https://doi.org/10.1016/s0927-0256(00)00194-4)
 49. Cleri F, Koblinski P, Colombo L, Phillpot SR, Wolf D (1998) Correlation between atomic structure and localized gap states in silicon grain boundaries. *Phys Rev B* 57:6247–6250. doi:[10.1103/PhysRevB.57.6247](https://doi.org/10.1103/PhysRevB.57.6247)
 50. Koblinski P, Phillpot SR, Wolf D, Gleiter H (1996) Thermodynamic criterion for the stability of amorphous intergranular films in covalent materials. *Phys Rev Lett* 77:2965–2968. doi:[10.1103/PhysRevLett.77.2965](https://doi.org/10.1103/PhysRevLett.77.2965)
 51. Koblinski P, Phillpot SR, Wolf D, Gleiter H (1997) On the thermodynamic stability of amorphous intergranular films in covalent materials. *J Am Ceram Soc* 80:717–732
 52. Koblinski P, Wolf D, Phillpot SR, Gleiter H (1998) Role of bonding and coordination in the atomic structure and energy of diamond and silicon grain boundaries. *J Mater Res* 13:2077–2099. doi:[10.1557/jmr.1998.0292](https://doi.org/10.1557/jmr.1998.0292)
 53. S Von Alfhthan, K Kaski, AP Sutton (2007) Molecular dynamics simulations of temperature-induced structural transitions at twist boundaries in silicon. *Phys Rev B* 76:245317. doi:[10.1103/PhysRevB.76.245317](https://doi.org/10.1103/PhysRevB.76.245317)
 54. Tarnow E, Dallot P, Bristowe PD, Joannopoulos JD, Francis GP, Payne MC (1990) Structural complexity in grain-boundaries with covalent bonding. *Phys Rev B* 42:3644–3657. doi:[10.1103/PhysRevB.42.3644](https://doi.org/10.1103/PhysRevB.42.3644)
 55. Cantwell PR, Tang M, Dillon SJ, Luo J, Rohrer GS, Harmer MP (2014) Grain boundary complexions. *Acta Mater* 62:1–48. doi:[10.1016/j.actamat.2013.07.037](https://doi.org/10.1016/j.actamat.2013.07.037)
 56. Mattheiss LF, Patel JR (1981) Electronic stacking-fault states in silicon. *Phys Rev B* 23:5384–5396. doi:[10.1103/PhysRevB.23.5384](https://doi.org/10.1103/PhysRevB.23.5384)